PHYSICAL REVIEW E **86**, 041602 (2012)

Electric-field-induced interfacial instabilities of a soft elastic membrane confined between viscous layers

Mohar Dey,[1] Dipankar Bandyopadhyay,[2] Ashutosh Sharma,[1,3,*] Shizhi Qian,[1,4] and Sang Woo Joo[1,†]
[1]*School of Mechanical Engineering, Yeungnam University, Gyeongsan 712-749, South Korea*
[2]*Department of Chemical Engineering, Indian Institute of Technology Guwahati, 781039, Assam, India*
[3]*Department of Chemical Engineering, Indian Institute of Technology Kanpur, UP 208016, India*
[4]*Institute of Micro/Nanotechnology, Old Dominion University, Norfolk, Virginia 23529, USA*
(Received 12 July 2012; published 10 October 2012)

We explore the electric-field-induced interfacial instabilities of a trilayer composed of a thin elastic film confined between two viscous layers. A linear stability analysis (LSA) is performed to uncover the growth rate and length scale of the different unstable modes. Application of a normal external electric field on such a configuration can deform the two coupled elastic-viscous interfaces either by an in-phase bending or an antiphase squeezing mode. The bending mode has a long-wave nature, and is present even at a vanishingly small destabilizing field. In contrast, the squeezing mode has finite wave-number characteristics and originates only beyond a threshold strength of the electric field. This is in contrast to the instabilities of the viscous films with multiple interfaces where both modes are found to possess long-wave characteristics. The elastic film is unstable by bending mode when the stabilizing forces due to the in-plane curvature and the elastic stiffness are strong and the destabilizing electric field is relatively weak. In comparison, as the electric field increases, a subdominant squeezing mode can also appear beyond a threshold destabilizing field. A dominant squeezing mode is observed when the destabilizing field is significantly strong and the elastic films are relatively softer with lower elastic modulus. In the absence of liquid layers, a free elastic film is also found to be unstable by long-wave bending and finite wave-number squeezing modes. The LSA asymptotically recovers the results obtained by the previous formulations where the membrane bending elasticity is approximately incorporated as a correction term in the normal stress boundary condition. Interestingly, the presence of a very weak stabilizing influence due to a smaller interfacial tension at the elastic-viscous interfaces opens up the possibility of fabricating submicron patterns exploiting the instabilities of a trilayer.

DOI: 10.1103/PhysRevE.86.041602 PACS number(s): 68.15.+e, 68.03.Cd, 81.16.Rf, 46.35.+z

I. INTRODUCTION

Interfacial instabilities of a thin soft polymer film can lead to interesting micron or submicron scale patterns, with potential applications in microfabrication, adhesives, optoelectronic or microfluidic devices, drug delivery components, and micro- and nanotextured functional interfaces such as superhydrophobic surfaces. In this context, the self-organized instabilities of thin viscous, viscoelastic, and elastic films engendered by the intermolecular forces [1–22] or externally applied electric field [23–35] are promising because they can lead to ordered patterns with the length scales ranging from a few microns to the submicron scales, when the field strength is tuned. In addition to the applications related to patterning, the thin film instabilities uncover key fundamental issues on the deformation and rupture of biological membranes [36–43], including injection [36], poration [37], and fusion [38–40] of vesicles and cells. Intensive research has thus been devoted for a better understanding of the instability and dynamics of thin films in the presence of various destabilizing fields.

Previous studies show that ultrathin liquid films (thickness $h_f < 100$ nm) can spontaneously dewet on a solid surface to form a collection of randomly placed droplets when the destabilizing intermolecular force ($\varphi \infty 1/h_f^4$) dominates over the stabilizing in-plane curvature force [1–22]. In contrast, the elastic stiffness imparts larger stability to the elastic films and the intermolecular force can overcome the combined stabilizing influences originating from the elastic and curvature forces only when a soft elastic film is thinner than a few nanometers [44]. For dewetting instabilities on homogeneous surfaces the "spinodal" length scale or spacing of the self-organized structures is decided by the imbalance of the stabilizing and destabilizing forces and is found to be a function of the film thickness (h_f) [7,9]. Similar to the dewetting scenario, thin liquid films can spontaneously develop contact instabilities on the surface when approached by an external contactor because of the adhesive intermolecular interaction between the film and the contactor [44]. However, the elastic films are unstable only below a threshold film-contactor gap (h_a), where the adhesive interaction ($\varphi \infty 1/h_a^4$) can dominate over the stabilizing surface tension and elastic forces [44–53]. The length scale of the contact instability for relatively thicker elastic films is linearly proportional to its thickness ($\lambda \sim 3h_f$), and is independent of its material properties [46,52]. However, for relatively thinner elastically soft films, surface tension also becomes important and the long-wave instability length scale here shows a nonlinear scaling with a nondimensional parameter, (γ/Gh_f), where γ is surface tension, G is elastic shear modulus, and h_f is the film thickness [34,44].

The film thickness (h_f) thus remains the single most important parameter for tuning of instabilities in elastic films. In this context, the interfacial instabilities originating from the external electric fields have the flexibility of tuning the

---

[*] ashutos@iitk.ac.in

[†] Author to whom correspondence should be addressed: swjoo@yu.ac.kr

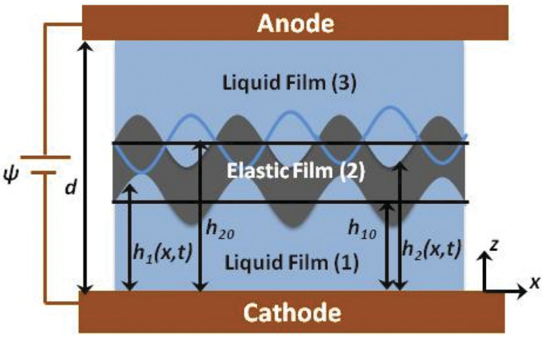

FIG. 1. (Color online) Schematic diagram of a confined trilayer under the influence of an electrostatic field of potential ψ, applied through an anode and a cathode separated by a distance d. The in-phase deformations at the interfaces depict a bending mode whereas an out-of-phase deformation shows the squeezing mode. The mean (local thicknesses) of the lower and upper liquid-liquid interfaces are h_{10} [$h_1(x,t)$] and h_{20} [$h_2(x,t)$], respectively.

destabilizing force by changing the external voltage bias [23–35]. Thin liquid films form interesting columnar structures with a hexagonal ordering at the free surface when exposed to an external electric field in which the spacing between the columns are decided by the net imbalance of the stabilizing surface tension and destabilizing electric field [30]. For an elastic film, the electric field has to overcome the additional elastic stiffness to develop similar morphologies on the film surface [33]. Previous studies indicate that for both intermolecular force [11–22,54–58] and the electric-field-induced [26–30,33] instabilities, a long-range order in the deformed structures can be observed when the bounding surfaces have arrays of periodic patterns with periodicity nearing the spinodal length scale. A number of recent studies show that in all the cases of thin film instabilities including dewetting [59–80], contact instability [81–84] and [54–58], and electric-field-induced instability [85–97] the use of multiple layers can add larger flexibility in terms of controlling the length scales and morphology. The interfacial instabilities of multilayers under the influence of electric field have the unique capability of producing a variety of embedded and encapsulated microstructures such as hierarchical core-shell structures [86,91,93] or phase inverted structures [87,91], which are otherwise difficult to pattern employing a conventional patterning technique or by means of other self-organization processes.

Here we study the electric-field-induced deformations of an elastic film confined between a pair of liquid films—a trilayer, as schematically shown in Fig. 1. The trilayer can be symmetric (asymmetric)—when the elastic film is surrounded by liquid films of same (different) thicknesses and physical properties. We perform a linear stability analysis (LSA) incorporating the full descriptions of the Maxwell's and hydrodynamic stresses and uncover the length and time scales of the different instability modes. The LSA shows that the pair of coupled elastic-viscous interfaces can undergo instability by two distinct modes: (i) a long-wave bending mode—where the interfaces deform in phase and (ii) a finite wave-number squeezing mode—when the interfaces evolve in antiphase. The analysis also reveals that these modes can have similar or dissimilar amplitudes of deformations at the interfaces under various conditions. The bending mode is found to be present under all conditions including when the destabilizing electric field is vanishingly small. In contrast, the inception of the finite wave-number squeezing mode requires a minimum destabilizing force. We establish the conditions when (i) only the bending mode is possible, (ii) a dominant bending mode coexists with a subdominant squeezing mode, and (iii) the squeezing mode dominates over a subdominant bending mode. We uncover the roles of elasticity, compliance, thickness of the elastic film, applied field strength, and ratio of viscosities and thicknesses of the liquid layers on the mode selection, length and time scales of instability, and the relative deformations at the interfaces because of these instabilities. We also discuss interesting asymptotic cases such as the deformation of a "free" elastic film sandwiched between a pair of electrodes and the effective bending elasticity of a thin elastic membrane confined between a pair of liquid layers. In this way, a justification for a previous analysis of the bending elasticity [41–43] is also provided. Unlike the previous works where the thin elastic film is treated as a small thickness membrane and the sole effect of its bending deformation is incorporated as a normal stress boundary condition [41–43], we consider the full description of the finite thickness elastic film and also uncover the results for the additional squeezing mode of deformation. The conditions in which submicron scale patterns can be developed have also been discussed to explore the possibilities of pattern miniaturization employing the trilayer configuration.

The rest of this paper is organized as follows. In Sec. II, we present the theoretical formulation for the electrohydrodynamic (EHD) fields and discuss linear stability analysis. In Sec. III, interesting results of consequence are discussed followed by concluding remarks in Sec. IV.

II. PROBLEM FORMULATION

In this section, the governing equations and boundary conditions are formulated for a trilayer consisting of a pair of liquid layers confining an elastic layer in the middle and subjected to a normal external electric field, as schematically shown in Fig. 1. The films are considered to be incompressible and perfectly dielectric materials. The liquid films are considered to be Newtonian whereas the elastic film is considered as a Hookean solid. The gravitational forces are neglected due to the small geometric scales considered in this study. For convenience, the films from bottom to top in Fig. 1 are termed as lower, middle, and upper layer, respectively. The films are also assumed to be isothermal and completely wettable on the substrates. The x and z coordinates are chosen to be in parallel and normal to the bottom substrate as shown in Fig. 1. The distance between the cathode and anode is denoted by d. The thicknesses of the lower layer, middle layer, and combined lower and middle layers are denoted by h_1, $h_M (= h_2 - h_1)$, and h_2, respectively. The corresponding base state thicknesses are denoted by h_{10}, h_{M0}, and h_{20}.

A. Model for electric field

For perfectly dielectric materials when the characteristic time for viscous flow is much larger than the electrically induced or magnetic effects, the electroneutrality prevails in the bulk, and the following conservation laws govern the electric field for the ith layer:

$$\nabla\cdot\mathbf{E}_i = 0, \tag{1}$$

$$\nabla\times\mathbf{E}_i = 0. \tag{2}$$

Here $\mathbf{E}_i = -\nabla\psi_i$ is the electric field, which can be expressed in terms of the gradient of the potential function ψ_i, when the electric field is irrotational [Eq. (2)]. The subscripts $i = 1, 2,$ and 3 in the expressions denote the lower viscous layer, middle elastic layer, and the upper viscous layer, respectively. Replacing the potential function in the governing equation Eq. (1) leads to the following Laplace equation for the ith layer:

$$\nabla^2\psi_i = 0. \tag{3}$$

The trilayer configuration shown in Fig. 1 ensures the zero-potential boundary condition at the cathode ($z = 0$):

$$\psi_1 = 0. \tag{4}$$

At the lower elastic-viscous interface ($z = h_1$), the normal and the tangential components of the electric field vector are balanced as follows:

$$\varepsilon_0\varepsilon_2(\mathbf{E}_2\cdot\mathbf{n}_1) - \varepsilon_0\varepsilon_1(\mathbf{E}_1\cdot\mathbf{n}_1) = 0, \tag{5}$$

$$\mathbf{E}_1\cdot\mathbf{t}_1 = \mathbf{E}_2\cdot\mathbf{t}_1. \tag{6}$$

At the upper elastic-viscous interface ($z = h_2$), the normal and the tangential component balances of the electric field vector are

$$\varepsilon_0\varepsilon_3(\mathbf{E}_3\cdot\mathbf{n}_2) - \varepsilon_0\varepsilon_2(\mathbf{E}_2\cdot\mathbf{n}_2) = 0, \tag{7}$$

$$\mathbf{E}_2\cdot\mathbf{t}_2 = \mathbf{E}_3\cdot\mathbf{t}_2. \tag{8}$$

At the anode ($z = d$) the electric potential boundary condition is

$$\psi_3 = \psi. \tag{9}$$

Here the notations $\mathbf{n}_j = [(1+h_{jx}^2)^{-1}\{-h_{jx},1\}]$ and $\mathbf{t}_j = [(1+h_{jx}^2)^{-1}\{1,h_{jx}\}]$ represent the unit outward normal and tangent vector at the interfaces, $z = h_j(x,t)$, where $j = 1$ and 2 represent lower and upper interfaces and the subscript x represents the derivative with respect to x. The symbols ε_i and ε_0 denote the relative permittivity of the ith layer and the permittivity in vacuum, respectively.

B. Model for hydrodynamic field

Owing to the relatively small thicknesses of the films, we ignore the effects of inertia and gravity on the fluid motion, and thus the following continuity and momentum equations govern the dynamics of the ith viscous layer ($i = 1$ and 3):

$$\nabla\cdot\mathbf{v}_i = 0, \tag{10}$$

$$-\nabla p_i + \nabla\cdot(\boldsymbol{\sigma}_i + \mathbf{M}_i) = 0. \tag{11}$$

Here $\boldsymbol{\sigma}_i = \mu_i(\nabla\mathbf{v}_i + \nabla\mathbf{v}_i^T)$ and $\mathbf{M}_i = \varepsilon_0\varepsilon_i[\mathbf{E}_i\otimes\mathbf{E}_i - 0.5(\mathbf{E}_i\cdot\mathbf{E}_i)\mathbf{I}]$ represent the hydrodynamic and the Maxwell stress tensor for the ith layer. The divergence of the Maxwell stress tensor is zero ($\nabla\cdot\mathbf{M}_i = 0$) because of the electroneutrality in the bulk. Therefore, the Maxwell's stress tensor will not affect momentum balance equations but will appear only in the interface boundary conditions. The symbols $\mathbf{v}_i[v_i^{(x)},v_i^{(z)}]$, p_i, and μ_i denote the velocity vector, isotropic static pressure, and viscosity of the ith layer, respectively. The bracketed superscript denotes the vector components.

The following conditions for incompressibility and equations of motion describe the dynamics of the middle elastic film ($i = 2$):

$$\nabla\cdot\mathbf{u}_i = 0, \tag{12}$$

$$-\nabla p_i + \nabla\cdot(\boldsymbol{\tau}_i + \mathbf{M}_i) = 0. \tag{13}$$

Here $\boldsymbol{\tau}_i = G(\nabla\mathbf{u}_i + \nabla\mathbf{u}_i^T)$ is the constitutive relation for a Hookean elastic solid and the symbols $\mathbf{u}_i[u_i^{(x)},u_i^{(z)}]$ and G denote the displacement vector and shear modulus of the middle elastic layer ($i = 2$). The EHD governing equations satisfy the no slip and impermeability boundary conditions at the cathode ($z = 0$) and anode ($z = d$):

$$\mathbf{v}_1 = 0, \tag{14}$$

$$\mathbf{v}_3 = 0. \tag{15}$$

At the lower elastic-viscous interface ($z = h_1$) the continuity of x and z directional velocities, normal and tangential stress balances are enforced as boundary conditions,

$$\mathbf{v}_1 = \mathbf{u}_{2t}, \tag{16}$$

$$\begin{aligned}&-p_1\mathbf{I} + \mathbf{n}_1\cdot(\boldsymbol{\sigma}_1 + \mathbf{M}_1)\cdot\mathbf{n}_1\\ &\quad + p_2\mathbf{I} - \mathbf{n}_1\cdot(\boldsymbol{\tau}_2 + \mathbf{M}_2)\cdot\mathbf{n}_1 = \gamma_{21}\kappa_1,\end{aligned} \tag{17}$$

$$\mathbf{t}_1\cdot(\boldsymbol{\sigma}_1 + \mathbf{M}_1)\cdot\mathbf{n}_1 - \mathbf{t}_1\cdot(\boldsymbol{\tau}_2 + \mathbf{M}_2)\cdot\mathbf{n}_1 = 0. \tag{18}$$

Here the subscript t represents the time derivative of the variable, the symbol $\kappa_j = \nabla\cdot\mathbf{n}_j$ denotes the curvature of the jth interface layer, and γ_{ij} represents the interfacial tension between the layers i and j. At the upper elastic-viscous interface ($z = h_2$), continuity of x and z directional velocities, normal and tangential stress balances are enforced as boundary conditions:

$$\mathbf{v}_3 = \mathbf{u}_{2t}, \tag{19}$$

$$\begin{aligned}&-p_2\mathbf{I} + \mathbf{n}_2\cdot(\boldsymbol{\tau}_2 + \mathbf{M}_2)\cdot\mathbf{n}_2 + p_3\mathbf{I} - \mathbf{n}_2\cdot(\boldsymbol{\sigma}_3 + \mathbf{M}_3)\cdot\mathbf{n}_2\\ &\quad = \gamma_{32}\kappa_2,\end{aligned} \tag{20}$$

$$\mathbf{t}_2\cdot(\boldsymbol{\tau}_2 + \mathbf{M}_2)\cdot\mathbf{n}_2 - \mathbf{t}_2\cdot(\boldsymbol{\sigma}_3 + \mathbf{M}_3)\cdot\mathbf{n}_2 = 0. \tag{21}$$

The kinematic conditions at the interfaces [$z = h_i(x,t)$, $i = 1$ and 2] can be expressed as

$$h_{it} + v_i^{(x)}h_{ix} = v_i^{(z)}. \tag{22}$$

Here the subscripts x and z in the expression denote the derivatives.

C. Linear stability analysis

A LSA for the trilayer has been performed on the quiescent base state expressed as $v_{i0}^{(x)} = v_{i0}^{(z)} = p_{i0} = 0$ for the viscous films and $u_{i0}^{(x)} = u_{i0}^{(z)} = p_{i0} = 0$ for the elastic film, with undisturbed film thicknesses h_{i0} under an electric field potential ψ_{i0} ($i = 1$, 2, and 3) given by

$$\psi_{i0zz} = 0. \tag{23}$$

Equation (23) has the general solution

$$\psi_{i0} = A_{1i}\, z + A_{2i}. \tag{24}$$

The constant for the base state potentials A_{ji} ($j = 1$ and 2; $i = 1$, 2, and 3) are obtained by enforcing $\psi_{10} = 0$ on the cathode ($z = 0$), $\varepsilon_0\varepsilon_1\psi_{10z} = \varepsilon_0\varepsilon_2\psi_{20z}$, and $\psi_{10} = \psi_{20}$ on the lower elastic-viscous interface ($z = h_{10}$), $\varepsilon_0\varepsilon_2\psi_{20z} = \varepsilon_0\varepsilon_3\psi_{30z}$, and $\psi_{20} = \psi_{30}$ on the upper elastic-viscous interface ($z = h_{20}$), and $\psi_{30} = \psi$, on the anode ($z = d$), where the subscripts z denote differentiation.

The governing equations and the boundary conditions described in Secs. II A and II B for the electric field and hydrodynamic field are linearized employing the normal modes $\mathbf{v_i} = \tilde{\mathbf{v}}_\mathbf{i} e^{\omega t + \mathbf{i}kx}$, $\mathbf{u_i} = \tilde{\mathbf{u}}_\mathbf{i} e^{\omega t + \mathbf{i}kx}$, $\psi_i = \psi_{i0} + \tilde{\psi}_i e^{\omega t + \mathbf{i}kx}$, $p_i = p_{i0} + \tilde{p}_i e^{\omega t + \mathbf{i}kx}$, and $h_i = h_{i0} + \tilde{\delta}_i e^{\omega t + \mathbf{i}kx}$, where ω and k denote the linear growth coefficient and the wave number of the disturbance, respectively. The variables $\tilde{\mathbf{v}}_\mathbf{i}$, $\tilde{\mathbf{u}}_\mathbf{i}$, $\tilde{\psi}_i$, and $\tilde{p}_i$ are the infinitesimal amplitudes of perturbations to the respective variables and are functions of z. The symbol $\tilde{\delta}_i$ represents the infinitesimal perturbation of height at the elastic-viscous interfaces. The governing equation for the linear perturbed potential function $\tilde{\psi}_i$ then is obtained as

$$\tilde{\psi}_{izz} - k^2\tilde{\psi}_i = 0. \tag{25}$$

Equation (25) has the general solution

$$\tilde{\psi}_i = C_{1i} e^{kz} + C_{2i} e^{-kz}. \tag{26}$$

Here the constants C_{ji} ($i = 1$, 2, and 3; $j = 1$, 2) are evaluated by considering the total potential ψ_i ($=\psi_{i0} + \tilde{\psi}_i$) for the ith layer and enforcing the boundary condition $\psi_1 = 0$ on the cathode ($z = 0$), normal ($\varepsilon_0\varepsilon_1\psi_{1z} = \varepsilon_0\varepsilon_2\psi_{2z}$ and $\varepsilon_0\varepsilon_2\psi_{2z} = \varepsilon_0\varepsilon_3\psi_{3z}$), and tangential ($\psi_1 = \psi_2$ and $\psi_3 = \psi_2$) component balances on the lower ($z = h_{10}$) and upper ($z = h_{20}$) elastic-viscous interfaces, and $\psi_3 = \psi$ on the anode ($z = d$).

The EHD governing equations for the viscous layers ($i = 1$ and 3) are linearized to

$$-\mathbf{i}k\tilde{p}_i + \mu_i\left(-k^2\tilde{v}_i^{(x)} + \frac{d^2\tilde{v}_i^{(x)}}{dz^2}\right) = 0, \tag{27}$$

$$-\frac{d\tilde{p}_i}{dz} + \mu_i\left(-k^2\tilde{v}_i^{(z)} + \frac{d^2\tilde{v}_i^{(z)}}{dz^2}\right) = 0, \tag{28}$$

$$\mathbf{i}k\tilde{v}_i^{(x)} + \frac{d\tilde{v}_i^{(z)}}{dz} = 0. \tag{29}$$

The EHD governing equations for the elastic layer ($i = 2$) are linearized as

$$-\mathbf{i}k\tilde{p}_2 + G\left(-k^2\tilde{u}_2^{(x)} + \frac{d^2\tilde{u}_2^{(x)}}{dz^2}\right) = 0, \tag{30}$$

$$-\frac{d\tilde{p}_2}{dz} + G\left(-k^2\tilde{u}_2^{(z)} + \frac{d^2\tilde{u}_2^{(z)}}{dz^2}\right) = 0, \tag{31}$$

$$\mathbf{i}k\tilde{u}_2^{(x)} + \frac{d\tilde{u}_2^{(z)}}{dz} = 0. \tag{32}$$

Eliminating $\tilde{p}_1$ and $\tilde{p}_3$ from the linearized governing equations [Eqs. (27)–(29)] for the two viscous layers and $\tilde{p}_2$ from Eqs. (30)–(32) yields the following biharmonic equations for the viscous layers and the elastic layer, respectively:

$$\frac{d^4\tilde{v}_i^{(z)}}{dz^4} - 2k^2\frac{d^2\tilde{v}_i^{(z)}}{dz^2} + k^4\tilde{v}_i^{(z)} = 0, \tag{33}$$

$$\frac{d^4\tilde{u}_i^{(z)}}{dz^4} - 2k^2\frac{d^2\tilde{u}_i^{(z)}}{dz^2} + k^4\tilde{u}_i^{(z)} = 0, \tag{34}$$

general solutions to which are

$$\tilde{v}_i^{(z)} = (B_{1i} + B_{2i}z)e^{kz} + (B_{3i} + B_{4i}z)e^{-kz}, \tag{35}$$

$$\tilde{u}_i^{(z)} = (B_{1i} + B_{2i}z)e^{kz} + (B_{3i} + B_{4i}z)e^{-kz}. \tag{36}$$

Here coefficients B_{ji} ($j = 1$ to 4; $i = 1$, 2, and 3) are constants. The general solutions for $\tilde{v}_i^{(z)}$ [Eq. (35)] and $\tilde{u}_i^{(z)}$ [Eq. (36)] lead to linear expressions for the remaining variables $\tilde{v}_i^{(x)}$, $\tilde{u}_i^{(x)}$, and $\tilde{p}_i$.

The boundary conditions for the EHD equations are also linearized using the normal modes. The resulting no slip and impermeability conditions at cathode ($z = 0$) and anode ($z = d$) are

$$\tilde{v}_1^{(x)} = \tilde{v}_1^{(z)} = 0, \tag{37}$$

$$\tilde{v}_3^{(x)} = \tilde{v}_3^{(z)} = 0. \tag{38}$$

At the lower elastic-viscous interface ($z = h_{10}$), the continuity of the x and z components of the velocities, the normal and the tangential stress balances, and the kinematic condition lead to

$$\tilde{v}_1^{(x)} = \omega\tilde{u}_2^{(x)}, \tag{39}$$

$$\tilde{v}_1^{(z)} = \omega\tilde{u}_2^{(z)}, \tag{40}$$

$$\begin{aligned}\tilde{p}_1 - \tilde{p}_2 - 2\mu_1\tilde{v}_{1z}^{(z)} + 2G\tilde{u}_{2z}^{(z)} + \varepsilon_0[(\varepsilon_2 A_{12}\tilde{\psi}_{2z})\\ -(\varepsilon_1 A_{11}\tilde{\psi}_{1z})] = \gamma_{21}k^2\tilde{\delta}_1,\end{aligned} \tag{41}$$

$$\mu_1\big(\tilde{v}_{1z}^{(x)} + \mathbf{i}k\tilde{v}_1^{(z)}\big) - G\big(\tilde{u}_{2z}^{(x)} + \mathbf{i}k\tilde{u}_2^{(z)}\big) = 0, \tag{42}$$

$$\tilde{\delta}_1 = \tilde{v}_1^{(z)}\big|_{h_{10}}/\omega. \tag{43}$$

On the upper elastic-viscous interface ($z = h_{20}$), the same conditions lead to

$$\tilde{v}_3^{(x)} = \omega\tilde{u}_2^{(x)}, \tag{44}$$

$$\tilde{v}_3^{(z)} = \omega\tilde{u}_2^{(z)}, \tag{45}$$

$$\begin{aligned}\tilde{p}_2 - \tilde{p}_3 - 2G\tilde{u}_{2z}^{(z)} + 2\mu_3\tilde{v}_{3z}^{(z)} + \varepsilon_0[(\varepsilon_3 A_{13}\tilde{\psi}_{3z})\\ -(\varepsilon_2 A_{12}\tilde{\psi}_{2z})] = \gamma_{32}k^2\tilde{\delta}_2,\end{aligned} \tag{46}$$

$$G\big(\tilde{u}_{2z}^{(x)} + \mathbf{i}k\tilde{u}_2^{(z)}\big) - \mu_3\big(\tilde{v}_{3z}^{(x)} + \mathbf{i}k\tilde{v}_3^{(z)}\big) = 0, \tag{47}$$

$$\tilde{\delta}_2 = \tilde{v}_3^{(z)}\big|_{h_{20}}/\omega. \tag{48}$$

Replacing the expressions of the variables $\tilde{v}_i^{(z)}$, $\tilde{v}_i^{(x)}$, $\tilde{u}_i^{(z)}$, $\tilde{u}_i^{(x)}$, and $\tilde{p}_i$ in the boundary conditions [Eqs. (37)–(48)], we obtain a set of twelve homogeneous linear algebraic equations with twelve unknown constants B_{ji} ($i = 1$, 2, and 3; $j = 1$ to 4). The determinant of the coefficient matrix of these algebraic equations leads to the dispersion relation listed in the Appendix. The analytical solution of the dispersion relation, $\omega = f(k)$, is a fourth order algebraic equation in ω and is solved analytically employing the symbolic package MATHEMATICA to obtain the real roots. The solutions of the dispersion relation corresponding to the bending and squeezing modes of instability are separated by specifying *a priori* the ratio of the deformation amplitudes as ± 1 ($\delta_r = \pm 1$) and then solving for ω. The neutral stability plots are obtained by setting $\omega = 0$ in the dispersion relation and then obtaining the critical wave number, k_c, from the resulting algebraic equation. The dominant growth coefficient (ω_m) and the corresponding wavelength ($\lambda_m = 2\pi/k_m$) are obtained by finding the global maxima of ω and the corresponding wave number k_m from the dispersion relation.

LSA is also used to predict the relative deformations corresponding to the squeezing and bending modes of instability at the interfaces for the confined trilayer (Fig. 1). Infinitesimal deformations α_2 and β_2 of the upper elastic-viscous interface in the x and z directions, respectively, are assumed initially. These deformations can be expressed in terms of the linear displacement of the upper elastic-viscous interface ($z = h_{20}$) as

$$\tilde{u}_2^{(x)} = \alpha_2, \quad \tilde{u}_2^{(z)} = \beta_2. \tag{49}$$

As a response to the infinitesimal deformation of the upper interface, the lower interface also deforms. Assuming the linearized x and z components of the infinitesimal displacements of the lower elastic-viscous interface ($z = h_{10}$) as α_1 and β_1, respectively, one can write

$$\tilde{u}_2^{(x)} = \alpha_1, \quad \tilde{u}_2^{(z)} = \beta_1. \tag{50}$$

Now using the boundary conditions, Eqs. (39)–(40) and Eqs. (44)–(45), we get

$$\tilde{v}_1^{(x)} = \omega\alpha_1, \quad \tilde{v}_1^{(z)} = \omega\beta_1, \tag{51}$$

$$\tilde{v}_3^{(x)} = \omega\alpha_2, \quad \tilde{v}_3^{(z)} = \omega\beta_2. \tag{52}$$

The coefficients B_{ji} ($j = 1$ to 4; $i = 1$, 2, and 3) in the general solution for $\tilde{v}_1^{(z)}$, $\tilde{u}_2^{(z)}$, and $\tilde{v}_3^{(z)}$, as already shown in Eqs. (35) and (36), are evaluated using the following boundary conditions: (i) at $z = 0$ and $z = d$, the no slip and impermeability conditions [Eqs. (37) and (38)]; (ii) at $z = h_{10}$ and h_{20}, the continuity of x and z component of velocities [Eqs. (49)–(52)]. For a given set of trilayer parameters, substituting the maximum linear growth coefficient (ω_m) and the corresponding wave number (k_m) into the expressions for B_{ji} ($j = 1$ to 4; $i = 1$, 2, and 3) makes them functions of α_1, α_2, β_1, and β_2 only. Subsequently, three out of the following four unused boundary conditions can be used to obtain the ratio δ_r ($=\beta_2/\beta_1$): (i) at $z = h_{10}$ and h_{20}, tangential stress balance [Eqs. (42) and (47)], and (ii) at $z = h_{10}$ and h_{20}, normal stress balance [Eqs. (41) and (46)]. δ_r gives information about the relative amplitudes of deformations at the two interfaces. The bending mode of instability can take place when $\delta_r > 0$ and the squeezing mode can develop at the interfaces when $\delta_r < 0$. Furthermore, the upper elastic-viscous interface has a larger amplitude of deformation when $|\delta_r| > 1$ whereas the lower interface deforms more when $|\delta_r| < 1$. The deformations of the coupled elastic-viscous interfaces can be of the same magnitude when $|\delta_r| = 1$, which is always the case for a symmetric system.

D. Special cases

The present formulation can be reduced to many interesting cases of asymptotic limits, such as a pair of viscous layers [58] or an elastic-viscous bilayer [84] under an electric field. Previous studies [41–43] on the deformation of an elastic membrane under an electric field consider a small thickness membrane, the bending elasticity of which can be incorporated in the normal stress boundary condition on the interface of a bilayer of viscous liquids. In this approach, the governing equations for the viscous films [Eqs. (10) and (11)] are considered together with the following continuity, normal and tangential stress balances, and the kinematic condition as the boundary conditions on the liquid-liquid interface ($z = h$):

$$\mathbf{v}_1 = \mathbf{v}_3, \tag{53}$$

$$\begin{aligned} &-p_1\mathbf{I} + \mathbf{n}\cdot(\boldsymbol{\sigma}_1 + \mathbf{M}_1)\cdot\mathbf{n} + p_3\mathbf{I} - \mathbf{n}\cdot(\boldsymbol{\sigma}_3 + \mathbf{M}_3)\cdot\mathbf{n} \\ &\quad = \gamma\kappa - B\nabla^2\kappa, \end{aligned} \tag{54}$$

$$\mathbf{t}\cdot(\boldsymbol{\sigma}_1 + \mathbf{M}_1)\cdot\mathbf{n} - \mathbf{t}\cdot(\boldsymbol{\sigma}_3 + \mathbf{M}_3)\cdot\mathbf{n} = 0. \tag{55}$$

$$h_t + v^{(x)}h_x = v^{(z)}. \tag{56}$$

The elastic film is modeled by the excess pressure contribution to the normal stress balance equation (54) due to a bending moment M at the interface $z = h(x,t)$, and appears as $\nabla^2 M$ where $M = B\nabla^2 h$ and $B = 2Gh_M^3/3(1-\nu)$, [98] where G, ν, and h_M denote the shear modulus, Poisson's ratio, and thickness of the elastic membrane, respectively, and γ ($=\gamma_{32} + \gamma_{21}$) represents the total interfacial tension. Figure 2 compares the LSA results obtained from the general analysis considering the trilayer configuration with an ultrathin (~10 nm) elastic layer to the results obtained from the approximate model [41–43] where the elastic film was modeled as a small thickness film. The curve (solid line) and the symbols (circles) in Fig. 2 show the growth coefficient (ω) vs wave-number (k) plots for the finite thickness and small thickness approximate model, respectively. The plot indeed shows that for all wave numbers, the approximate model (with small thickness elastic membrane) accurately predicts

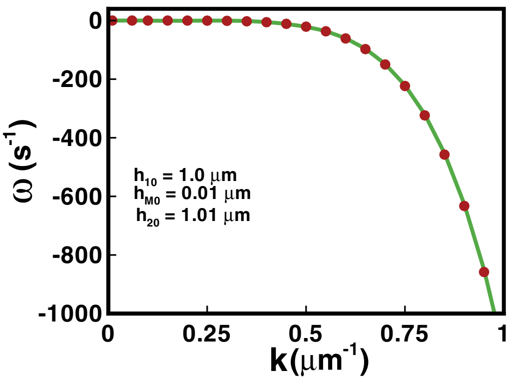

FIG. 2. (Color online) Linear stability analysis (LSA) results comparing the general and the simplified [Eq. (54)] analyses of the bending elasticity. The solid line and the symbols (circles) correspond to the finite thickness and small thickness elastic membrane, respectively. The other parameters are $h_{10} = 1.0\ \mu$m, $h_{20} = 1.01\ \mu$m, $d = 2.01\ \mu$m, $\varepsilon_1 = 15$, $\varepsilon_2 = 7$, $\varepsilon_3 = 18$, $\mu_1 = \mu_3 = 0.001$ Pa s, $\gamma_{21} = \gamma_{32} = 0$, $\psi = 0$, and $G = 100$ MPa.

the contribution of bending elasticity in the dispersion relation. The approximate model could only predict purely bending deformation without any change in thickness, which is not always the case as can be seen in the discussion for the next figure.

Another interesting asymptotic case we discuss here is when the elastic layer is free to deform surrounded by a non-viscous fluid such as air under the influence of the external electric field. In such a situation, the following Laplace equation governs the electric field distribution across the elastic layer:

$$\nabla^2 \psi_2 = 0. \tag{57}$$

However, the zero-potential boundary condition is enforced on the lower elastic-air interface ($z = h_{10}$), which acts as the cathode,

$$\psi_2 = 0. \tag{58}$$

On the anode ($z = h_{20}$),

$$\psi_2 = \psi. \tag{59}$$

The EHD formulation for this system is the same as the trilayer configuration described in the previous sections with the bounding liquid layers assumed to be nonviscous gases.

III. RESULTS AND DISCUSSION

Application of an electrostatic field across a dielectric material accumulates induced dipoles and develops additional electrical stresses on the interface. As a measure of stress relaxation, any soft interface without permanent elasticity

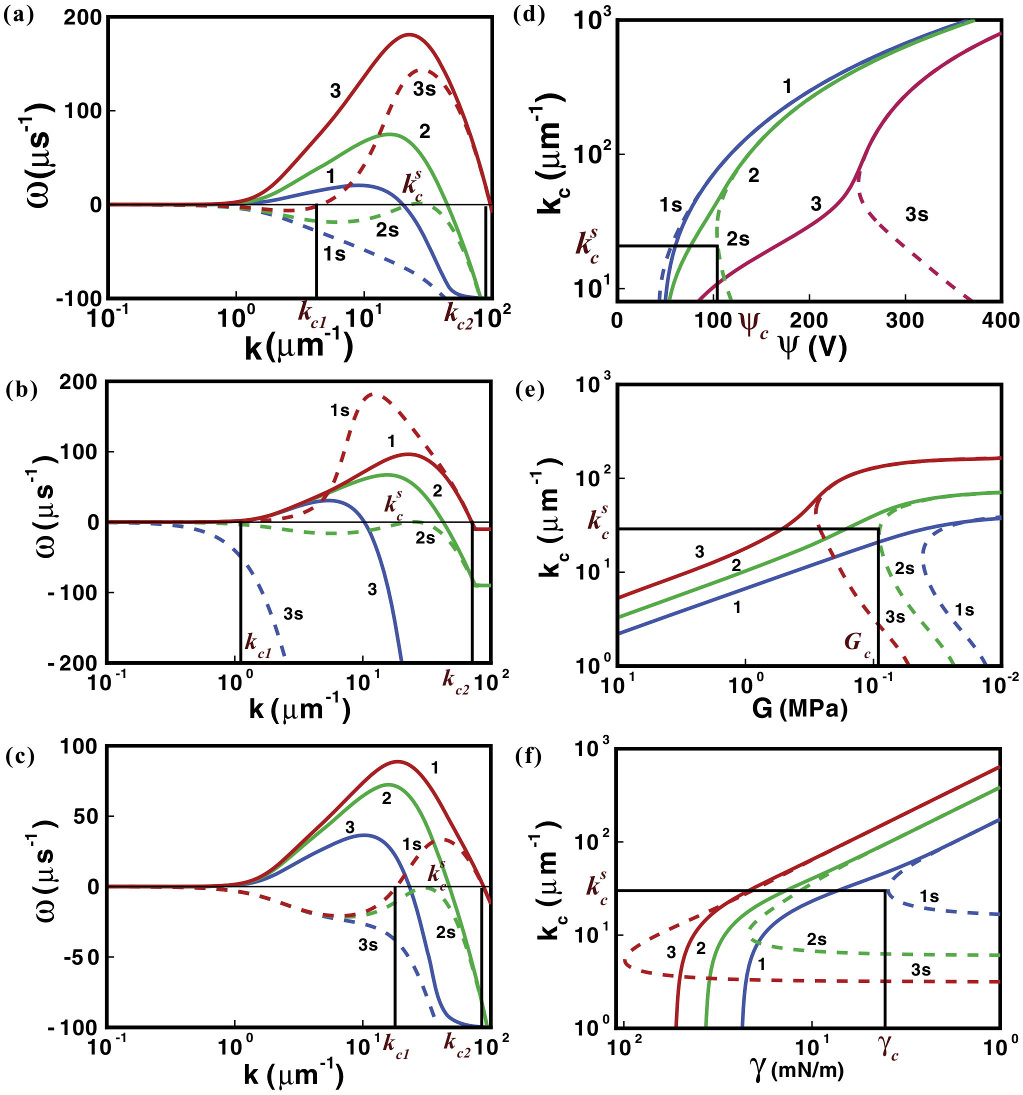

FIG. 3. (Color online) LSA results for the symmetric configuration. The solid and broken lines correspond to the bending and squeezing modes. Plots (a)–(c) show the variation of ω with k when ψ, G, and γ are varied. Plots (d)–(f) show the variation of k_c with ψ, G, and γ, respectively. Curves 1–3 correspond to $\psi = 75$, 104, and 135 V, when $G = 0.1$ MPa in plot (a); to $G = 0.01$, 0.09, and 1 MPa, when $\psi = 100$ V in plot (b); and to $\gamma_{21} = \gamma_{32} = \gamma = 0.002$, 0.004, and 0.01 N m^{-1}, when $\psi = 100$ V in plot (c). In plot (d), curves 1–3 correspond to $G = 0.01$, 0.1, and 1 MPa whereas in plot (e), curves 1–3 correspond to $\psi = 75$, 100, and 150 V. In plot (f), curves 1–3 correspond to $\psi = 100$, 125, and 150 V, when $G = 0.1$ MPa.

such as a liquid-air or a liquid-liquid interface spontaneously deforms to displace the material with the lower dielectric permittivity. However, we will show that for an elastic layer, a finite force is required for the onset of deformations that produce a local change in the film thickness (squeezing mode). Further, although a vanishingly small electric field can spontaneously deform the elastic-viscous interfaces into a pure bending mode without any change in the local thickness, a critical field strength is required to engender a bending mode of instability with unequal amplitudes at the elastic-viscous interfaces. Likewise, for the antiphase squeezing mode or any out-of-phase mixed mode of deformations, a minimum destabilizing force is required to overcome the elastic strain energy of the elastic film. Various thermodynamic and kinetic parameters such as the ratios of the dielectric permittivites, viscosities, and thickness of the films; interfacial tensions at the interfaces; the elasticity of the films; and the applied field strength play key roles in influencing the nature of interfacial deformations and the patterns formed. In the following discussion, we explore the effects of all these parameters on the onset of the instability and on the time and length scales of instabilities in the trilayer. For convenience the trilayers are classified into (i) symmetric—when the bounding liquid layers are identical, and (ii) asymmetric—when the bounding viscous layers are dissimilar. The results for these symmetric and asymmetric configurations are compared and contrasted to uncover the salient features of the interfacial instabilities of a trilayer. Unless otherwise noted, the parameters employed for the analysis are $h_{10} = 1.0\ \mu$m, $h_{20} = 1.1\ \mu$m, $d = 2.1\ \mu$m, $\varepsilon_2 = 4$, $\varepsilon_1 = \varepsilon_3 = 15$, $\mu_1 = \mu_3 = 0.001$ Pa s, $\gamma_{21} = \gamma_{32} = 0.005$/N/m, $\psi = 100$ V, and $G = 0.1$ MPa. The physical properties are chosen according to a realistic trilayer configuration with a soft-elastic poly-dimethylsiloxane (PDMS) film confined by purely dielectric (de-ionized) waterlike layers.

Figure 3 summarizes the LSA results on the inception and dominance of the bending and squeezing modes of the instabilities for a symmetric configuration. The plots (a)–(c) show the ω vs k plots with variations in ψ, G, and γ, respectively. The plots (d)–(f) show neutral stability plots or the bifurcation diagrams with variations in ψ, G, and γ, respectively. The solid curves 1–3 in all the plots confirm that the bending mode of instability has indeed the long-wave ($\omega \rightarrow 0$ as $k \rightarrow 0$) characteristics. In contrast, the broken curves 1s–3s in the plots indicate that the squeezing mode bifurcates at a finite wave number such that $\omega > 0$ only for a range of wave numbers, $k_{c1} < k < k_{c2}$ where $k_{c1} \neq 0$. The curves also show that the most natural mode of destabilization is the bending mode because it is present under all conditions. In contrast, curves 1s–3s in Figs. 3(a) and 3(d) show that as the strength of the electric field increases, the squeezing mode appears beyond a threshold field strength. The bifurcation diagrams with broken lines in Fig. 3(d) indicate that with increase in the elastic stiffness of the middle layer, the critical field strength (Ψ_c) required for an unstable squeezing mode also increases. Further, curves 1 and 1s in Fig. 3(b) shows that when the elastic film is sufficiently soft (0.01 MPa), the squeezing

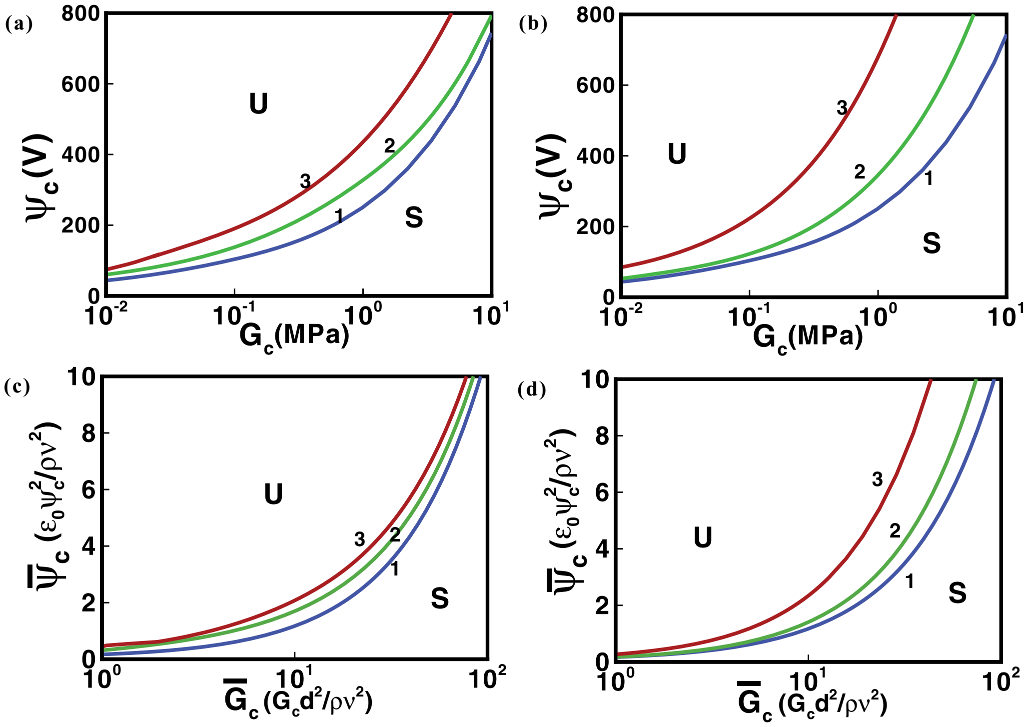

FIG. 4. (Color online) Stability diagrams depicting the stable and unstable regions for the symmetric trilayer. Plots (a) and (b) show the variation of ψ_c with G_c when γ and $h_{M0}(=h_{20} - h_{10})$ are varied. Plots (c) and (d) show the variation $\bar{\psi}_c$ with $\bar{G}_c$ when H_{M0} and Γ are varied keeping d constant. Curves 1–3 correspond to $\gamma_{21} = \gamma_{32} = \gamma = 0.005, 0.05$, and 0.5 N/m in plot (a) and to $h_{M0} = 0.1, 0.5$, and $2\ \mu$m, in plot (b). In plot (c), curves 1–3 correspond to $\Gamma_{21} = \Gamma_{32} = \Gamma = 0.0105, 0.105$, and 0.21, and to $H_{M0} = 0.0471, 0.095$, and 0.23 in plot (d). In plots (a) and (c), $h_{10} = 1.0\ \mu$m, $h_{20} = 1.1\ \mu$m, and $d = 2.1\ \mu$m and in plots (b) and (d), $d = 2.1\ \mu$m, and $\gamma_{21} = \gamma_{32} = 0.005$ N/m.

mode can become the dominant mode in the presence of a subdominant bending mode. However, curves 3 and 3s in Fig. 3(b) show when the elastic restoring force is sufficiently high ($G \sim 1$ MPa), the bending mode is the fastest mode growing with a subdominant squeezing mode. The bifurcation diagrams 1s–3s in Fig. 3(e) indicate that higher elasticity films (higher G_c) require higher field strength for the onset of the squeezing mode. Figure 3(c) shows that increase in the interfacial tensions at the interfaces can suppress the squeezing mode of instability and can again promote a dominant bending mode. The bifurcation plots in Fig. 3(f) show that with increase in the strength of the destabilizing field the critical interfacial tension (γ_c) for the appearance of the squeezing mode increases. The plots in Fig. 3 confirm that the long-wave bending is present under all conditions, whereas the squeezing modes can appear only beyond a critical destabilizing force. The critical wave number at which the squeezing mode appears is denoted as k_c^s in the bifurcation diagrams Figs. 3(a)–3(f). The inception of the squeezing mode delays as the electric field becomes weaker and the elastic stiffness at the interfaces gains strength. The plots for a symmetric trilayer also indicate that even if the squeezing mode is present, it is not always the dominant mode of instability. The squeezing mode is found to be dominant when either the applied field is very strong or the elastic resistance is very weak.

Figure 4 shows parametric plots for a symmetric trilayer where the domains of stability or instability for the squeezing mode have been identified by varying the dimensional $\mathbf{\Psi}_c$ and G_c [plots (a) and (b)] and nondimensional $\bar{\mathbf{\Psi}}_c$ and $\bar{G}_c$ [plots (c) and (d)]. In plots (a) and (b), the parameters γ and h_{M0} $(=h_{20}-h_{10})$ are varied by keeping d constant and in plots (c) and (d) the dimensionless middle layer thickness $(H_{M0}=h_{M0}/d)$ and surface tension $(\Gamma=\gamma d/\rho \nu^2)$ are varied. The regions marked "U" and "S" are the zones where unstable and stable squeezing modes are present. The plots clearly indicate that the squeezing mode is favored at higher electric field strength and at lower elasticity. The plots also show that with increase in thickness of the elastic layer and the interfacial tensions at the interface, the critical force required to initiate the squeezing mode instability increases. The results shown here will aid future experiments involving the trilayers discussed in this study.

Figures 5–8 show the influence of the applied voltage (ψ), dielectric permittivity (ε_2), the shear modulus (G), and the compliance of the elastic film ($C=h_{M0}/G$) on the mode selection as well as on the length and time scales of instabilities for the symmetric trilayer configurations. Figure 5 depicts the transition of the dominant mode—from bending to squeezing or vice versa with ψ. Plot (a) shows the growth coefficient (ω) vs wave-number (k) diagrams, plots (b) and (c) show the variations in the dominant growth coefficient (ω_m) and the corresponding wavelength (λ_m) with ψ, and plot (d) shows the variation in the ratio of amplitudes of deformations (δ_r) at the two interfaces with ψ. For a constant ε_2 and G, Figs. 5(a)–5(c) show that increase in ψ leads to a reduction in time (increasing ω_m) and length (decreasing λ_m) scales. Figure 5(c)

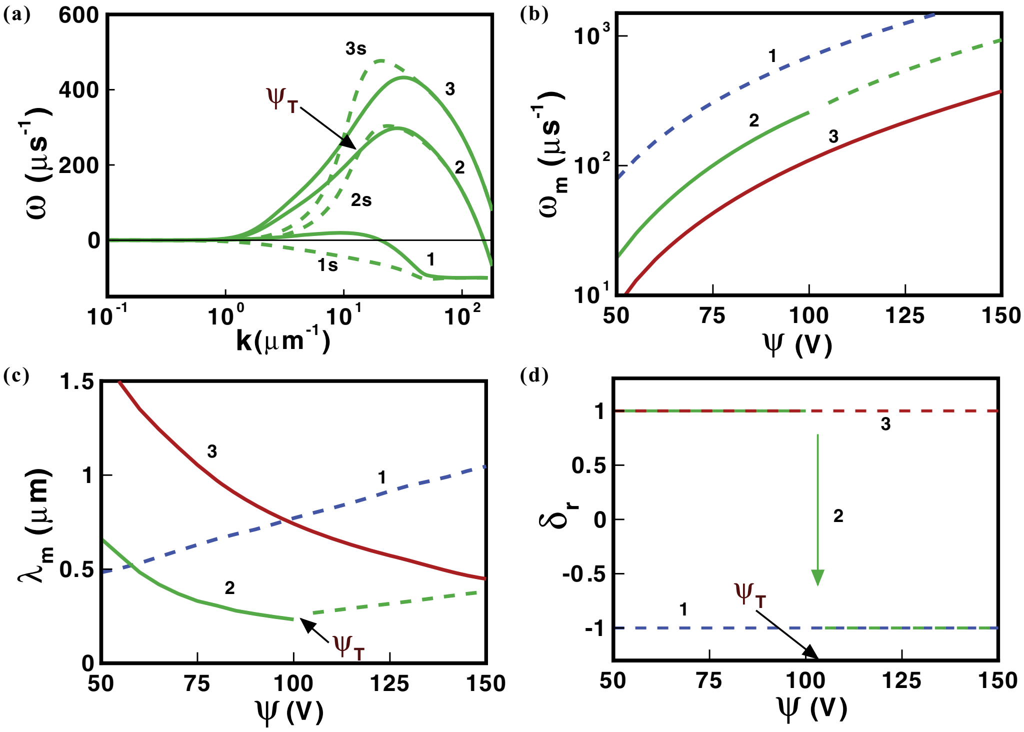

FIG. 5. (Color online) Plot (a) shows the variation of ω with k where curves 1–3 correspond to $\psi=50$, 105, and 120 V, respectively, with constant $G=0.1$ MPa and $\varepsilon_2=2$. Plots (b)–(d) show the variations of ω_m, λ_m, and δ_r with ψ where curves 1–3 correspond to $G=0.01$, 0.1, and 1 MPa when $\varepsilon_2=2$. The solid and broken lines in plots (a)–(c) correspond to the bending and squeezing modes. The transition potential $\mathbf{\Psi}_T$ marks the point of transition between the two modes in plots (a), (c), and (d). The downward vertical arrow (2) in plot (d) shows the transition from bending to squeezing mode.

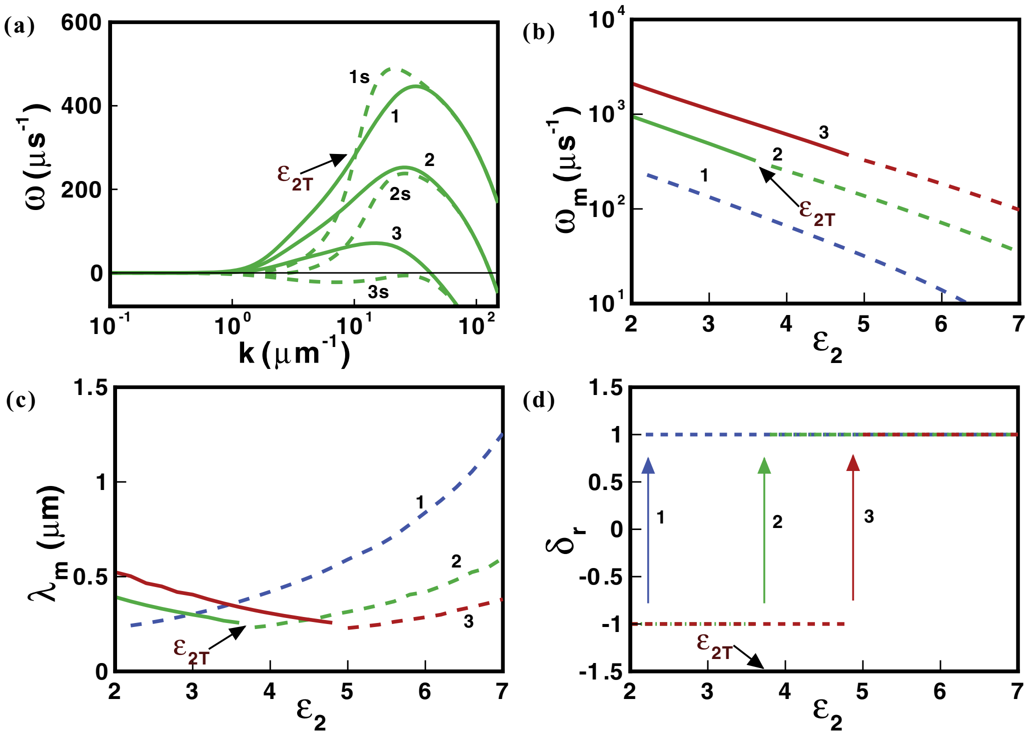

FIG. 6. (Color online) Plot (a) shows the variation of ω with k where curves 1–3 correspond to $\varepsilon_2 = 3.8$, 4, and 6 when $G = 0.095$ MPa and $\psi = 150$ V. Plots (b)–(d) show the variations of ω_m, λ_m, and δ_r with ε_2 where curves 1–3 correspond to $\psi = 100$, 150, and 200 V when $G = 0.095$ MPa. The solid and broken lines in plots (a)–(c) correspond to the bending and squeezing modes. The transitional dielectric permittivity $\boldsymbol{\varepsilon}_{2T}$ marks the point of transition between the two modes in plots (a)–(d). The upward vertical arrows (1–3) in plot (d) show the switching from squeezing to bending mode.

emphasizes that the lower resistance from the elastic stiffness can even reduce the length scale to a few hundred nanometers. Curve 2 in plots (c) and (d) suggests that when the elastic stiffness is low, a transition from dominant bending mode (solid line) to a dominant squeezing mode (broken line) takes place at a transition voltage ($\boldsymbol{\Psi}_{\mathrm{T}}$). The discontinuities in Fig. 5(d) with arrows show the transition point from the bending ($\delta_r = 1$) to squeezing modes ($\delta_r = -1$) of instabilities more clearly. Interestingly, at the transition point the length scale reaches the minimum value, which indicates that when both modes have equal strength, the pattern spacing can achieve the smallest possible length scale for a trilayer.

Figure 6 summarizes the LSA results when the dielectric permittivity ε_2 of the elastic film is varied. Figure 6(a) shows the typical ω vs k plots, and Figs. 6(b)–6(d) show the variations of ω_m, λ_m, and δ_r with ε_2 for different values of ψ. Figures 6(a)–6(c) show that with increasing ε_2 the strength of the destabilizing electrical forces decreases because of the decreasing dielectric contrast across the two interfaces, which in turn decreases ω_m and increases λ_m. Figure 6(d) shows the transition from squeezing to bending mode of instability that occurs at a transition dielectric permittivity, ε_{2T}. Again, Fig. 6(c) depicts that the length scale is minimum at the transition point when both the instability modes are equally strong. The minimum length scale is of the order of a few hundred nanometers. Curves 1 and 2 in Fig. 6(d) show that with the reduction in the dielectric permittivity of the elastic film, the increased dielectric contrast at the interfaces enhances the electrical stresses, which eventually helps in the shift from bending ($\delta_r = 1$) to squeezing ($\delta_r = -1$) mode at a much lower applied field than when the dielectric permittivity of the elastic film is high and the trilayer needs a much stronger applied field for the transition.

Figure 7 depicts the transition of the dominant modes of deformations from bending to squeezing or vice versa with the change in G. Figure 7(a) shows the typical ω vs k plots, and Figs. 7(b)–7(d) show the variations of ω_m, λ_m, and δ_r with G. The solid curves indicate that the bending mode [$\delta_r = 1$ in Fig. 7(d)] is the preferred one when the elastic stiffness is high. The broken curves confirm that when the elastic resistance reduces, the squeezing mode can be the dominant mode [$\delta_r = -1$ in Fig. 7(d)]. The points of discontinuities with the notations G_T show the transition from the dominant squeezing to dominant bending mode with the change in the elastic modulus G.

Figure 8 summarizes the LSA results when the compliance of the elastic film is varied. The compliance of the film is defined as the ratio of the elastic film thickness to its shear modulus ($C = h_{M0}/G$). Figure 8(a) shows the typical ω vs k plots, and Figs. 8(b)–8(d) show the variations of ω_m, λ_m, and δ_r with the compliance of the film. For a constant ε_2 and ψ, Figs. 8(a)–8(c) show that with decreasing G and increasing compliance (C) of the elastic film, the strength of the stabilizing elastic forces at the two interfaces decreases considerably leading to an increase in ω_m and decrease in λ_m. Figures 8(b) and 8(c) show that as C is increased, for thicker

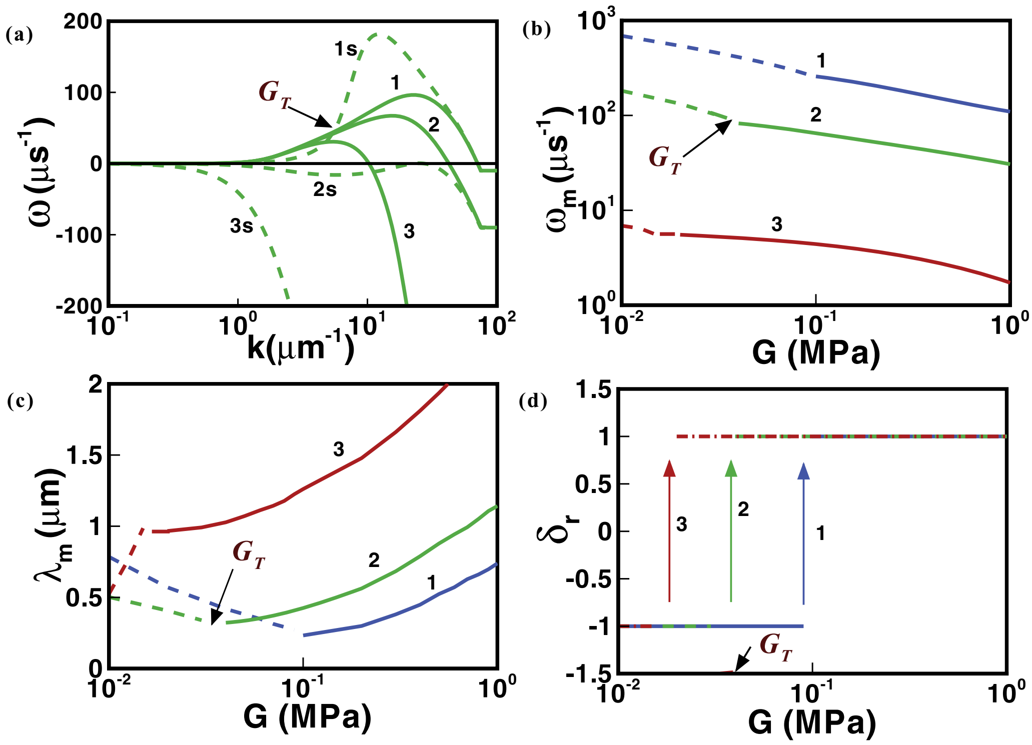

FIG. 7. (Color online) Plot (a) shows the variation of ω with k where curves 1–3 correspond to $G = 0.01$, 0.09, and 1 MPa, when $\psi = 100$ V and $\varepsilon_2 = 4$. Plots (b)–(d) show the variation of ω_m, λ_m, and δ_r with G, where curves 1–3 correspond to $\varepsilon_2 = 2$, 4, and 7, respectively, at $\psi = 100$ V. The solid and broken lines in plots (a)–(c) correspond to the bending and squeezing modes. The transitional shear modulus $\mathbf{G}_T$ marks the changeover from squeezing to bending mode in plots (a)–(d). The upward vertical arrows (1–3) in plot (d) show the transition from squeezing to bending mode.

films (higher h_{M0}), the stabilizing elastic force is increased to a greater extent and the elastic film becomes less compliant to the destabilizing electrical force, thus decreasing ω_m and increasing λ_m. The points of discontinuities with the notations C_T [in Fig. 8(d)] shows the transition from the dominant bending mode to dominant squeezing mode with the change in the compliance C of the elastic film. The plot marked (d) in all the Figs. 5–8 shows that the symmetric trilayer can only lead to a symmetric bending or a symmetric squeezing mode of instabilities in which the amplitudes of deformations at the interfaces are same.

Figure 9 shows the LSA results for the asymmetric trilayers. These figures depict the variations in ω_m, λ_m, and δ_r with the ratios of the film thicknesses, $h_r(=h_{30}/h_{10})$, dielectric permittivities, $\varepsilon_r(=\varepsilon_3/\varepsilon_1)$, interfacial tensions, $\gamma_r(=\gamma_{32}/\gamma_{21})$, and viscosities $\mu_r(=\mu_3/\mu_1)$ of the liquid films. Figures 9(a)–9(c) show the effect of h_r, Figs. 9(d)–9(f) show the effect of ε_r, Figs. 9(g)–9(i) show the effect of variation of γ_r, and Figs. 9(j)–9(l) show the effect of variation of μ_r. For $\varepsilon_1 > \varepsilon_3$, curves marked 1 in Figs. 9(a) and 9(b) show that ω_m and λ_m decreases with increasing h_r because with increase in the thickness of the upper viscous film (increasing h_r) and resulting decrease in the thickness of the lower viscous film with higher dielectric permittivity, the electric stresses at the lower interface increases and this reduces the time and length scales of instability. This results in the lower interface deforming more in comparison to the upper interface as shown by curve 1 in Fig. 9(c). However, when the permittivities at the liquid layers are the same (curve 2, $\varepsilon_1 = \varepsilon_3$) increase in thickness of any of the liquid layers does not change the length and the time scales because the stabilizing and the destabilizing stresses remain invariant. Furthermore, when $\varepsilon_3 > \varepsilon_1$, curve 3 shows that the increase in the thickness of the upper film with higher dielectric permittivity (increasing h_r) increases the destabilizing electrical stresses at the interfaces to increase ω_m and reduce λ_m. Figure 9(c) shows that for smaller values of h_r, the amplitudes of deformations at the interfaces remain similar as $|\delta_r| = 1$ and a symmetric bending ($\delta_r = 1$) or squeezing ($\delta_r = -1$) mode is expected. When $\varepsilon_1 = \varepsilon_3$ (curve 2), an exclusive bending mode can be expected whereas for the cases $\varepsilon_1 < \varepsilon_3$ or $\varepsilon_1 > \varepsilon_3$ the squeezing mode prevails as the dominant mode of instability (curves 1 and 3). Interestingly, in the case of $\varepsilon_3 > \varepsilon_1$ (curve 3), with increase in the upper layer thickness (increasing h_r), the upper interface deforms with a larger amplitude ($\delta_r < -1$) and an asymmetric squeezing mode of instability is present.

Figures 9(d)–9(f) show a very interesting transition when ε_r is varied for different values of μ_r. Curve 1 in these plots depict that when the lower layer permittivity is highest and the upper layer has permittivity almost similar to the middle layer, the interfaces evolve in a bending mode with smaller deformation at the upper interface ($0 < \delta_r < 1$). The larger deformation at the lower layer can be attributed to the larger dielectric contrast across the lower interface. The time and length scales

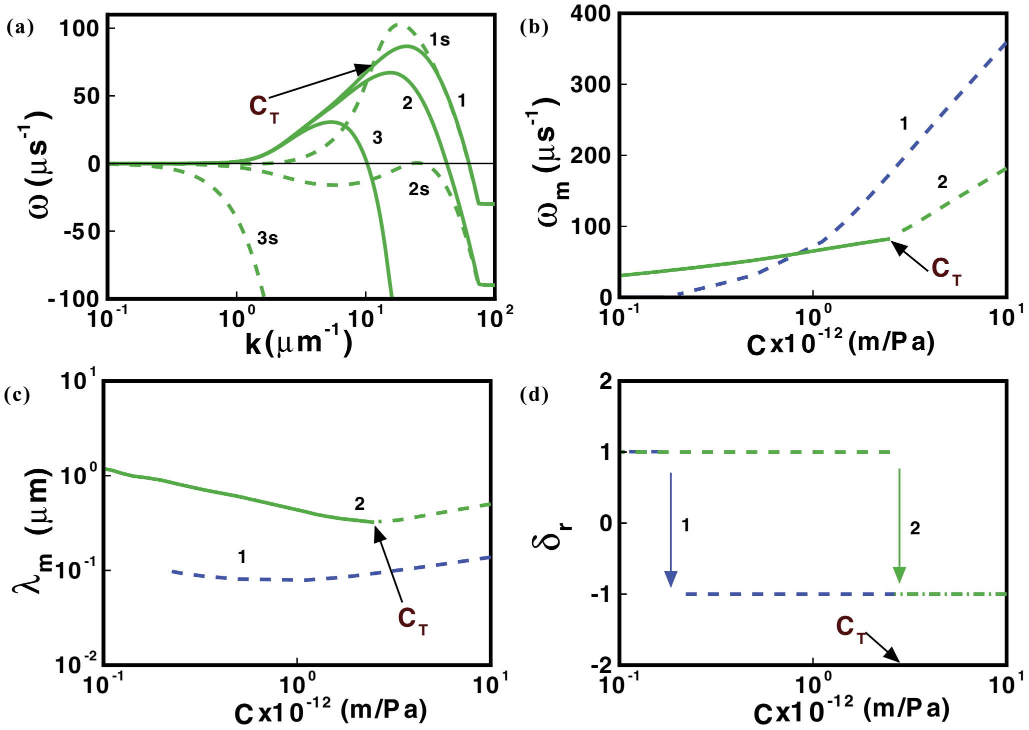

FIG. 8. (Color online) Plot (a) shows the variation of ω with k where curves 1–3 correspond to compliance C $(=h_{M0}/G)$=10, 3.3, 0.1 ($\times$ 10^{-12}) m/Pa, when $\psi = 100$ V and $\varepsilon_2 = 4$. Plots (b)–(d) show the variations of ω_m, λ_m, and δ_r with G, where curves 1 and 2 correspond to $h_{M0} = 10$ and 100 nm, respectively. The solid and broken lines in plots (a)–(c) correspond to the bending and squeezing modes. The transitional compliance $\mathbf{C}_T$ marks the point of transition between the two modes in plots (a)–(d). The downward vertical arrows (1 and 2) in plot (d) show the switching from bending to squeezing mode.

progressively reduce with increase in ε_3 and the upper interface progressively deforms more ($\delta_r > 1$) because of the lesser viscous resistance surrounding it. With further increase in ε_3 a transition from bending ($\delta_r > 0$) to squeezing ($\delta_r < 0$) mode of instability is observed, as shown by the point of discontinuity in curve 1 of Fig. 9(f). Importantly, in this squeezing mode of deformation the upper interface deforms more ($|\delta_r| \gg 1$) due to the smaller viscous resistance across the upper interface. However, at higher values of ε_3, which reduces the dielectric contrast across the interfaces, a more symmetric squeezing mode can be observed because δ_r values approach -1. It is also important to note here that the length scale again shows a minimum near the point of transition from the squeezing to bending mode, as shown by curve 1 in Fig. 9(e). Curves 2 and 3 in these plots show that when the upper interface is kinetically stabilized by increasing the viscous resistance across it, the transitions observed in the previous case can be totally suppressed and an asymmetric bending or squeezing mode with larger deformation at the lower interface is the only possibility. This is shown by curves 2 and 3 in the inset of Fig. 9(f).

Figures 9(g)–9(i) show the variations of the length and time scales of instability at different ε_r as the ratio of the interfacial tensions (γ_r) is varied. The plots in Figs. 9(g) and 9(h) show that changing γ_r can also significantly alter the length and the time scales. For example, curve 3 in these plots shows that increasing the interfacial tension at the upper interface can lead to increase in length and time scales of instability as the stabilizing influence increases. In this situation, a larger dielectric contrast and a lower interfacial tension can cause a larger deformation ($|\delta_r| \gg 1$) across the upper interface as compared to the lower interface, as shown by curve 3 in Fig. 9(i). Interestingly, a smaller elastic stiffness causes a squeezing mode ($\delta_r < -1$) of instability under this condition. In contrast to these observations, curves 1 and 2 in these plots show that a larger dielectric contrast causes a larger deformation to the lower interface ($0 < |\delta_r| \ll 1$) as shown in the inset of Fig. 9(i). In such a scenario, increasing the interfacial tension at the upper interface has very little influence on the length and time scales.

Figures 9(j)–9(l) show the effects of the ratio of the viscosities of the upper to lower liquid layer, μ_r, on the length and the time scales and on the relative amplitudes on the two interfaces for different values of γ_r. It may be noted that changing the viscosity ratio can significantly alter the kinetics of growth instability at the two interfaces. As is evident from Figs. 9(j)–9(l), curves 1 show that at low μ_r (low μ_3) the smaller viscous resistance together with a weaker stabilizing influence from the interfacial tension leads to a bending mode of instability with a larger deformation at the upper interface. With increase in the viscous resistance, the deformations on the two interfaces become similar as δ_r approaches 1 at higher values of μ_r in Fig. 9(l). In comparison, curve 2 shows that when the interfacial tension at the interfaces are equal, increasing viscous resistance at the upper layer can not only suppress the growth of the deformation on the

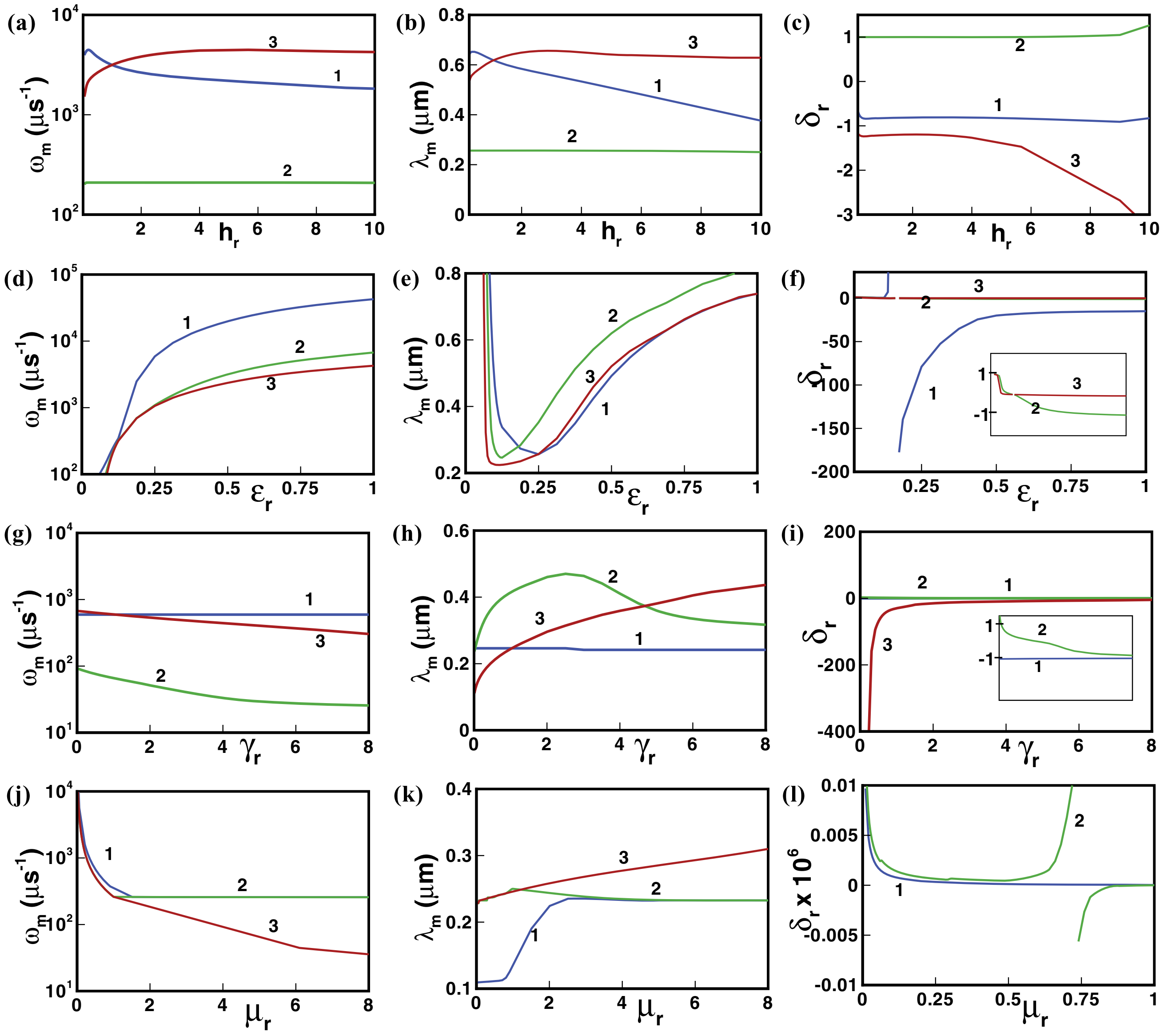

FIG. 9. (Color online) LSA results for the asymmetric configuration. Plots [(a),(b),(c)], [(d),(e),(f)], [(g),(h),(i)], and [(j),(k),(l)] show the variations of [ω_m, λ_m, δ_r] with h_r, ε_r, γ_r, and μ_r, respectively. In plots (a)–(c) the curves 1–3 correspond to $\varepsilon_r = 0.5$, 1, and 2, respectively, when $h_{M0} = 0.1$ μm. In plots (d)–(f) the curves 1–3 correspond to $\mu_r = 0.1$, 1, and 10, respectively, when $\varepsilon_1 = 80$, $\varepsilon_2 = 4$. In plots (g)–(i) the curves 1–3 correspond to $\varepsilon_r = 0.25$, 1, and 4, respectively, when $G = 0.095$ MPa. Curves 1–3 in plots (j)–(l) represent $\gamma_r = 0.01$, 1, and 10, respectively, when $G = 0.095$ MPa.

upper interface but also also cause a transition of modes from bending to squeezing when the viscosity of the upper layer is high. The transition is depicted by the discontinuity of curve 2 in Fig. 9(l). Figure 9 depicts the various possibilities of the asymmetric deformations of the coupled interfaces in the forms of either a long-wave asymmetric bending mode or a finite wave-number squeezing mode. The plot highlights the relative strength of the interfacial tensions on the interfaces and the ratios of the viscosity, dielectric permittivity, and thickness of the liquid layer on the mode selection and the subsequent length and time scales of the electric-field-induced instabilities in the trilayer. Similar to the symmetric trilayer scenario, the length scale plots in Figs. 9(b), 9(e), 9(h), and 9(k) show that the patterns on ~100-nm elastic layers can be of the order of a few hundred nanometers, which opens up the possibility of fabricating submicron patterns exploiting the instabilities of this configuration.

Figure 10 shows the neutral stability plots for the asymptotic case where an elastic film deforms freely under the influence of a destabilizing external electric field applied by directly keeping the two interfaces at constant potentials. In the absence of viscous influences, the competition between the stabilizing elastic and capillary forces and the destabilizing electric field dictates the length scale for this system. Curves 1 in plots (a) and (b) show the bifurcation diagrams with the change in the applied potential $\Delta\psi$ across the elastic film and the

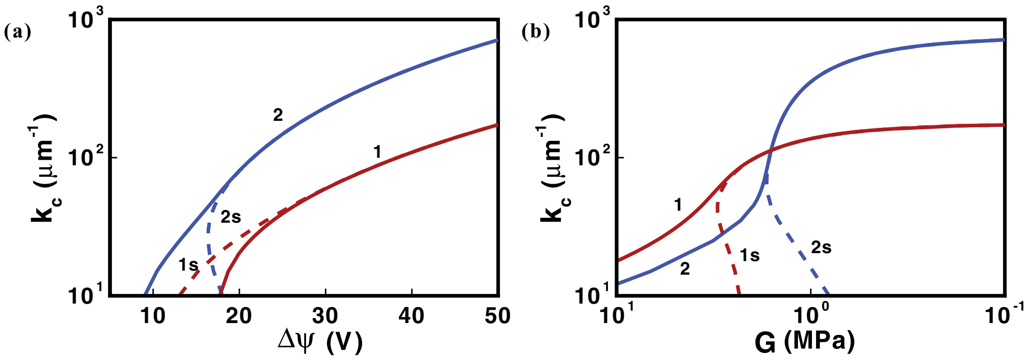

FIG. 10. (Color online) The solid and broken lines correspond to the bending and squeezing modes. Plots (a) and (b) show the variation of k_c with $\Delta\psi$ and G, respectively. Curves 1 and 2 in these plots correspond to the cases with fixed applied potential at the elastic-air interfaces and at the electrodes, respectively. In plot (a), $G = 0.1$ MPa and in plot (b), $\Delta\psi = 50$ V. For the surface applied potential, $\gamma_{21} = \gamma_{32} = 0.05$ N/m and $\mu_1 = \mu_3 = 0$, and for the externally applied potential $\gamma_{21} = \gamma_{32} = 0.005$ N/m and $\mu_1 = \mu_3 = 0.001$ Pa s.

shear modulus (G) of the film, respectively, for the free elastic layer. The results for the free elastic layer are compared and contrasted with the trilayer under consideration in curve 2. The solid and broken curves in the plots indicate that similar to the trilayer the free elastic layer can also be unstable by the long-wave bending and finite wave-number squeezing modes of instabilities. Similar to the trilayers, the bending mode can be present under all conditions whereas the squeezing mode appears beyond a threshold field strength. Curves 1 and 2 in plot (a) show that the critical field ($\Delta\Psi$) required for the inception of the unstable squeezing mode is smaller for the trilayer configuration as compared to the free elastic film because the interfaces of a trilayer have much lower stabilizing interfacial tension as compared to the free elastic layer. For the same reason the critical shear modulus (G) required for the inception of the unstable squeezing mode is higher for the free elastic film than the similar trilayer configuration, as shown in Fig. 10(b). Plots (a) and (b) also show that the span of unstable wave numbers is much larger for the trilayer than for a free layer because of the presence of the weaker stabilizing interfacial tensions on the interfaces. The weaker interfacial tensions allow a span of unstable wave numbers in the larger wave-number regime for the trilayer.

IV. CONCLUSIONS

The electric-field-induced instabilities in a trilayer comprised of an elastic film confined between two viscous layers is investigated using linear stability analysis (LSA). In addition to analyzing the length and time scales of instabilities, this study highlights a number of salient features of the trilayer configuration. The major contributions of this study can be summarized as follows.

The pair of coupled elastic-viscous interfaces can undergo either an in-phase bending deformation or an antiphase squeezing deformation when exposed to an external electric field. The bending mode has a long-wave nature and exists for all strengths of the destabilizing force, whereas the squeezing mode bifurcates at a finite wave number and only beyond a critical force. The trilayers are classified as symmetric or asymmetric based on the similarity or dissimilarity of the bounding liquid layers. A minimum destabilizing force is also necessary for the inception of the bending mode where the amplitudes of deformations at the two interfaces are unequal in an asymmetric trilayer. The bending mode of instability is favored by weak destabilizing fields and by stronger stabilizing elastic and surface tension forces. In comparison, a squeezing mode is favored when the elastic stiffness of the middle film is relatively low and the applied field strength is relatively high. The conditions for the coexistence of the dominant (subdominant) bending (squeezing) modes are also discussed.

In the asymmetric systems, transition from the bending to squeezing mode can be tuned by changing the ratios of dielectric permittivities, viscosities, thicknesses, and the surface tensions of the liquid layers. These parameters are also found to significantly influence the amplitude of deformations at the two interfaces. For example, increasing the viscosity of a liquid layer slows down the growth of instability at the proximal interface, whereas increase in the dielectric contrast across an interface causes greater destabilization by increasing the strength of the destabilizing field. A number of examples of the mode transitions and also of the tuning of the interfacial amplitudes have been discussed. Importantly, for most of the cases, the length scale is found to attain a minimum under the conditions when both the modes are equally strong, which signals the point of mode transition.

The study also highlights that the minimum length scale of instabilities for a ∼100-nm-thick elastic layer can reach as low as a few hundred nanometers, which underlines the possibility of fabricating submicron patterns by exploiting the electric-field-induced interfacial instabilities in elasto-viscous trilayers. The instability near the point of the minimum length scale has a short-wave characteristic which can only be resolved by a general finite wave-number formulation presented here, but not by a long-wave analysis. Interestingly, this analysis recovers the results of previously simplified bending elasticity formulations where the elastic film is modeled as a small thickness film with a correction term in the normal stress boundary condition [41–43]. The formulation outlined in this study can also be used effectively to obtain the explicit expression for the bending elasticity contribution when the coupled elastic-viscous interfaces deform in squeezing mode. The present formulation is all encompassing in that it not only recovers all the results of the approximate formulations but also predicts the long, short, and finite wave-number characteristics of the symmetric and asymmetric bending and squeezing modes and their transitions.

In summary, we have presented an analysis to motivate experiments on patterning of elastic layers embedded in viscous fluids, such as the instabilities in synthetic and biological membranes confined by external electric fields. The focus here has been on the linear stability analysis of the incompressible and dielectric films. The compressibility and electrical conductivity can also play important roles. In addition, nonlinear effects including the geometric nonlinearity of the elastic film become important when surface deformations become large. It is hoped that the present formalism will motivate future works in these areas.

ACKNOWLEDGMENT

This work is supported by the World Class University Grant No. KRF R32-2008-000-20082-0 of the National Research Foundation of Korea.

APPENDIX

The linear dispersion relation is the following 12 × 12 determinant:

$$\begin{vmatrix}
1 & -1 & \frac{1}{k} & \frac{1}{k} & 0 & 0 & 0 & 0 & 0 & 0 & 0 & 0 \\
1 & 1 & 0 & 0 & 0 & 0 & 0 & 0 & 0 & 0 & 0 & 0 \\
J_1 & -J_2 & J_1 J_5 & -J_2 J_6 & -\omega J_1 & \omega J_2 & -\omega J_1 J_5 & \omega J_2 J_6 & 0 & 0 & 0 & 0 \\
J_1 & J_2 & h_1 J_1 & h_1 J_2 & -\omega J_1 & -\omega J_2 & -\omega h_1 J_1 & -\omega h_1 J_2 & 0 & 0 & 0 & 0 \\
-2k\mu_1 J_1 & -2k\mu_1 J_2 & -2k\mu_1 J_1 J_5 & -2k\mu_1 J_2 J_6 & 2kG_2 J_1 & 2kG_2 J_2 & 2kG_2 J_1 J_5 & 2kG_2 J_2 J_6 & 0 & 0 & 0 & 0 \\
J_1 J_9 & J_2 J_{10} & h_1 J_1 J_9 & h_1 J_2 J_{10} & 2kG_2 J_1 & -2kG_2 J_2 & 2kh_1 G_2 J_1 & -2kh_1 G_2 J_2 & \frac{J_3\phi_2}{\omega} & \frac{J_4\phi_2}{\omega} & \frac{h_2 J_3\phi_2}{\omega} & \frac{h_2 J_4\phi_2}{\omega} \\
0 & 0 & 0 & 0 & -\omega J_3 & \omega J_4 & -\omega J_3 J_7 & \omega J_4 J_8 & J_3 & -J_4 & J_3 J_7 & -J_4 J_8 \\
0 & 0 & 0 & 0 & -\omega J_3 & -\omega J_4 & -\omega h_2 J_3 & -\omega h_2 J_4 & J_3 & J_4 & h_2 J_3 & h_2 J_4 \\
0 & 0 & 0 & 0 & -2kG_2 J_3 & -2kG_2 J_4 & -2kG_2 J_3 J_7 & -2kG_2 J_4 J_8 & 2k\mu_3 J_3 & 2k\mu_3 J_4 & 2k\mu_3 J_3 J_7 & 2k\mu_3 J_4 J_8 \\
\frac{J_1\phi_4}{\omega} & \frac{J_2\phi_4}{\omega} & \frac{h_1 J_1\phi_4}{\omega} & \frac{h_1 J_2\phi_4}{\omega} & -2kG_2 J_3 & 2kG_2 J_4 & -2kh_2 G_2 J_3 & 2kh_2 G_2 J_4 & J_3 J_{11} & J_4 J_{12} & h_2 J_3 J_{11} & h_2 J_4 J_{12} \\
0 & 0 & 0 & 0 & 0 & 0 & 0 & 0 & e^{dk} & -e^{dk} & \frac{e^{dk}(1+dk)}{k} & \frac{-e^{-dk}(-1+dk)}{k} \\
0 & 0 & 0 & 0 & 0 & 0 & 0 & 0 & e^{dk} & e^{-dk} & de^{dk} & de^{-dk}
\end{vmatrix} = 0.$$

Here the notation corresponds to

$$J_1 = e^{kh_1},\quad J_2 = e^{-kh_1},\quad J_3 = e^{kh_2},\quad J_4 = e^{-kh_2},\quad J_5 = \frac{(1+kh_1)}{k},\quad J_6 = \frac{(-1+kh_1)}{k},\quad J_7 = \frac{(1+kh_2)}{k},$$

$$J_8 = \frac{(-1+kh_2)}{k},\quad J_9 = \frac{(\phi_1 - 2\omega k\mu_1)}{\omega},\quad J_{10} = \frac{(\phi_1 + 2\omega k\mu_1)}{\omega},\quad J_{11} = \frac{(\phi_3 + 2\omega k\mu_3)}{\omega},\quad J_{12} = \frac{(\phi_3 - 2\omega k\mu_3)}{\omega},$$

$$\phi_1 = \left(-\gamma_{21}k^2 + \frac{\partial\pi_1}{\partial h_1}\right),\quad \phi_2 = \left(\frac{\partial\pi_2}{\partial h_1}\right),\quad \phi_3 = \left(-\gamma_{32}k^2 + \frac{\partial\pi_2}{\partial h_2}\right),\quad \phi_4 = \left(\frac{\partial\pi_1}{\partial h_2}\right),$$

$$\pi_1 = \frac{\varepsilon_0}{2}\left[\varepsilon_2\left(\frac{\partial\psi_2}{\partial z}\right)^2 - \varepsilon_1\left(\frac{\partial\psi_1}{\partial z}\right)^2\right]\Bigg|_{z=h_1},\quad \pi_2 = \frac{\varepsilon_0}{2}\left[\varepsilon_3\left(\frac{\partial\psi_3}{\partial z}\right)^2 - \varepsilon_2\left(\frac{\partial\psi_2}{\partial z}\right)^2\right]\Bigg|_{z=h_2}.$$

[1] E. Ruckenstein and R. K. Jain, J. Chem. Soc., Faraday Trans. 2 **70**, 132 (1974).
[2] P. G. de Gennes, Rev. Mod. Phys. **57**, 827 (1985).
[3] G. Reiter, Phys. Rev. Lett. **68**, 75 (1992).
[4] F. Brochard-Wyart, P. Martin, and C. Redon, Langmuir **9**, 3682 (1993).
[5] A. Sharma, Langmuir **9**, 861 (1993).
[6] A. Oron, S. H. Davis, and S. G. Bankoff, Rev. Mod. Phys. **69**, 931 (1997).
[7] A. Sharma and R. Khanna, Phys. Rev. Lett. **81**, 3463 (1998).
[8] U. Thiele, M. G. Velarde, and K. Neuffer, Phys. Rev. Lett. **87**, 016104 (2001).
[9] R. V. Craster and O. K. Matar, Rev. Mod. Phys. **81**, 1131 (2009).
[10] A. Patra, D. Bandyopadhyay, G. Tomar, A. Sharma, and G. Biswas, J. Chem. Phys. **134**, 064705 (2011).
[11] R. Konnur, K. Kargupta, and A. Sharma, Phys. Rev. Lett. **84**, 931 (2000).
[12] K. Kargupta and A. Sharma, Phys. Rev. Lett. **86**, 4536 (2001).
[13] L. Brusch, H. Kühne, U. Thiele, and M. Bär, Phys. Rev. E **66**, 011602 (2002).

[14] N. Savva, S. Kalliadasis, and G. A. Pavliotis, Phys. Rev. Lett. **104**, 084501 (2010).
[15] A. Sehgal, V. Ferreiro, J. F. Douglas, E. J. Amis, and A. Karim, Langmuir **18**, 7041 (2002).
[16] D. H. Kim, M. J. Kim, J. Y. Park, and H. H. Lee, Adv. Funct. Mater. **15**, 1445 (2005).
[17] J. H. Wei, D. C. Coffey, and D. S. Ginger, J. Phys. Chem. B **110**, 24324 (2006).
[18] G. G. Baralia, C. Filiatre, B. Nysten, and A. M. Jones, Adv. Mater. **19**, 4453 (2007).
[19] C. P. Martin, M. O. Blunt, E. Pauliac-Vaujour, A. Stannard, P. Moriarty, I. Vancea, and U. Thiele, Phys. Rev. Lett. **99**, 116103 (2007).
[20] D. Julthongpiput, W. H. Zhang, J. F. Douglas, A. Karim, and M. J. Fasolka, Soft Matter **3**, 613 (2007).
[21] R. Mukherjee, D. Bandyopadhyay, and A. Sharma, Soft Matter **4**, 2086 (2008).
[22] L. Xuea and Y. Hana, Prog. Polym. Sci. **36**, 269 (2011).
[23] E. Schäffer, T. Thurn-Albrecht, T. P. Russell, and U. Steiner, Nature (London) **403**, 874 (2000).
[24] P. Deshpande, X. Sun, and S. Y. Chou, Appl. Phys. Lett. **79**, 1688 (2001).
[25] S. Harkema and U. Steiner, Adv. Funct. Mater. **15**, 2016 (2005).
[26] N. E. Voicu, S. Harkema, and U. Steiner, Adv. Funct. Mater. **16**, 926 (2006).
[27] N. Wu, L. F. Pease III, and W. B. Russel, Adv. Funct. Mater. **16**, 1992 (2006).
[28] N. E. Voicu, S. Ludwigs, and U. Steiner, Adv. Mater. **20**, 3022 (2008).
[29] L. F. Pease III and W. B. Russel, Langmuir **21**, 12290 (2005).
[30] R. Verma, A. Sharma, K. Kargupta, and J. Bhaumik, Langmuir **21**, 3710 (2005).
[31] N. Wu and W. B. Russel, Nano Today **4**, 180 (2009).
[32] G. Tomar, V. Shankar, A. Sharma, and G. Biswas, J. Non-Newtonian Fluid Mech. **43**, 120 (2007).
[33] J. Sarkar, A. Sharma, and V. B. Shenoy, Phys. Rev. E **77**, 031604 (2008).
[34] N. Arun, A. Sharma, P. S. G. Pattader, I. Banerjee, H. M. Dixit, and K. S. Narayan, Phys. Rev. Lett. **102**, 254502 (2009).
[35] V. A. Kishore and D. Bandyopadhyay, J. Phys. Chem. C **116**, 6215 (2012).
[36] M. Winterhalter and W. Helfrich, J. Phys. Chem. **92**, 6865 (1988).
[37] H. N. W. Lekkerkerker, Physica A **159**,319 (1989).
[38] T. Chou, M. Jaric, and E. Siggia, Biophys. J. **72**, 2042 (1997).
[39] T. Ambjornsson, M. A. Lomholt, and P. L. Hansen, Phys. Rev. E **75**, 051916 (2007).
[40] J. Schwalbe, P. M. Vlahovska, and M. J. Miksis, Phys. Fluids **23**, 041701 (2011).
[41] D. Lacoste, M. C. Lagomarsino, and J. F. Joanny, Europhys. Lett. **77**,18006 (2007).
[42] D. Lacoste, G. I. Menon, M. Z. Bazant, and J. F. Joanny, Eur. Phys. J. E: Soft Matter Biol. Phys. **28**, 243 (2009).
[43] F. Ziebert, M. Z. Bazant, and D. Lacoste, Phys. Rev. E **81**, 031912 (2010).
[44] J. Sarkar and A. Sharma, Langmuir **26**, 8464 (2010).
[45] A. Ghatak, M. K. Chaudhury, V. Shenoy, and A. Sharma, Phys. Rev. Lett. **85**, 4329 (2000).
[46] V. Shenoy and A. Sharma, Phys. Rev. Lett. **86**, 119 (2001).
[47] C. Q. Ru, J. Appl. Phys. **90**, 6098 (2001).
[48] W. Mönch and S. Herminghaus, Europhys. Lett. **53**, 525 (2001).
[49] V. Shenoy and A. Sharma, J. Mech. Phys. Solids **50**, 1155 (2002).
[50] J. Sarkar, V. Shenoy, and A. Sharma, Phys. Rev. Lett. **93**, 018302 (2004).
[51] J. Yoon, C. Q. Ru, and A. Midouchowski, J. Appl. Phys. **98**, 113503 (2005).
[52] M. Gonuguntla, A. Sharma, J. Sarkar, S. A. Subramanian, M. Ghosh, and V. Shenoy, Phys. Rev. Lett. **97**, 018303 (2006).
[53] M. Gonuguntala, A. Sharma, R. Mukharjee, and S. A. Subramanian, Langmuir **22**, 7066 (2006).
[54] M. Gonuguntala, A. Sharma, and S. A. Subramanian, Macromolecules **39**, 3365 (2006).
[55] J. Y. Chung, K. Kim, M. K. Chaudhury, J. Sarkar, and A. Sharma, Eur. Phys. J. E: Soft Matter Biol. Phys. **20**, 47 (2006).
[56] R. C. Pangule, I. Banerjee, and A. Sharma, J. Chem. Phys. **128**, 234708 (2008).
[57] R. Mukherjee, R. C. Pangule, A. Sharma, and I. Banerjee, J. Chem. Phys. **127**, 064703 (2007).
[58] A. Sharma, M. Gonuguntla, R. Mukherjee, S. A. Subramanian, and R. C. Pangule, J. Nanosci. Nanotechnol. **7**, 1744 (2007).
[59] A. M. Higgins and R. A. L. Jones, Nature **404**, 476 (2000).
[60] R. A. Segalman and P. F. Green, Macromolecules **32**, 801 (1999).
[61] J. Léopoldès and P. Damman, Nat. Mater. **5**, 957 (2006).
[62] J. P. de Silva, M. Geoghegan, A. M. Higgins, G. Krausch, M. O. David, and G. Reiter, Phys. Rev. Lett. **98**, 267802 (2007).
[63] K. D. Danov, V. N. Paunov, N. Alleborn, H. Raszillier, and F. Durst, Chem. Eng. Sci. **53**, 2809 (1998).
[64] K. D. Danov, V. N. Paunov, S. D. Stoyanov, N. Alleborn, H. Raszillier, and F. Durst, Chem. Eng. Sci. **53**, 2823 (1998).
[65] V. N. Paunov, K. D. Danov, N. Alleborn, H. Raszillier, and F. Durst, Chem. Eng. Sci. **53**, 2839 (1998).
[66] A. Pototsky, M. Bestehorn, D. Merkt, and U. Thiele, Phys. Rev. E **70**, 025201 (2004).
[67] S. Kumar and O. K. Matar, J. Colloid Interface Sci. **273**, 581 (2004).
[68] O. K. Matar, V. Gkanis, and S. Kumar, J. Colloid Interface Sci. **286**, 319 (2005).
[69] D. Bandyopadhyay, R. Gulabani, and A. Sharma, Ind. Eng. Chem. Res. **44**, 1259 (2005).
[70] A. Pototsky, M. Bestehorn, D. Merkt, and U. Thiele, J. Chem. Phys. **122**, 224711 (2005).
[71] L. S. Fisher and A. A. Golovin, J. Colloid Interface Sci. **291**, 515 (2005).
[72] D. Bandyopadhyay and A. Sharma, J. Chem. Phys. **125**, 054711 (2006).
[73] A. Pototsky, M. Bestehorn, D. Merkt, and U. Thiele, Europhys. Lett. **74**, 665 (2006).
[74] A. A. Nepomnyashchy and I. B. Simanovskii, Phys. Fluids **18**, 112101 (2006).
[75] A. A. Nepomnyashchy and I. B. Simanovskii, Phys. Fluids **18**, 032105 (2006).
[76] L. S. Fisher and A. A. Golovin, J. Colloid Interface Sci. **307**, 203 (2007).
[77] R. D. Lenz and S. Kumar, J. Colloid Interface Sci. **316**, 660 (2007).
[78] D. Bandyopadhyay and A. Sharma, J. Phys. Chem. B **112**, 11564 (2008).
[79] D. Bandyopadhyay, A. Sharma, and C. Rastogi, Langmuir **24**, 14048 (2008).

[80] A. A. Nepomnyashchy and I. B. Simanovskii, J. Fluid Mech. **631**, 165 (2009).

[81] D. Bandyopadhyay, A. Sharma, and V. Shankar, J. Chem. Phys. **128**, 154909 (2008).

[82] G. Tomar, A. Sharma, V. Shenoy, and G. Biswas, Phys. Rev. E **76**, 011607 (2007).

[83] R. Mukherjee, R. Pangule, A. Sharma, and G. Tomar, Adv. Func. Mater. **17**, 2356 (2007).

[84] D. Bandyopadhyay, A. Sharma, and V. Shankar, Europhys. Lett. **89**, 36002 (2010).

[85] Z. Lin, T. Kerle, S. M. Baker, D. A. Hoagland, E. Schaffer, U. Steiner, and T. P. Russell, J. Chem. Phys. **114**, 2377 (2001).

[86] M. D. Morariu, N. E. Voicu, E. Schäffer, Z. Lin, T. P. Russell, and U. Steiner, Nat. Mater. **2**, 48 (2003).

[87] K. A. Leach, S. Gupta, M. D. Dickey, C. G. Wilson, and T. P. Russell, Chaos **15**, 047506 (2005).

[88] V. Shankar and A. Sharma, J. Colloid Interface Sci. **274**, 294 (2004).

[89] R. V. Craster and O. K. Matar, Phys. Fluids **17**, 032104 (2005).

[90] S. A. Roberts and S. Kumar, J. Fluid Mech. **631**, 255 (2009).

[91] D. Bandyopadhyay, A. Sharma, U. Thiele, and P. D. S. Reddy, Langmuir **25**, 9108 (2009).

[92] S. Srisvastava, D. Bandyopadhyay, and A. Sharma, Langmuir **26**, 10943 (2010).

[93] P. D. S. Reddy, D. Bandyopadhyay, and A. Sharma, J. Phys. Chem. C **114**, 21020 (2010).

[94] S. A. Roberts and S. Kumar, Phys. Fluids **22**, 122102 (2010).

[95] A. Atta, D. G. Crawford, C. R. Koch, and S. Bhattacharjee, Langmuir **27**, 12472 (2011).

[96] P. G. Oppenheimer, S. Mahajan, and U. Steiner, Adv. Opt. Mater. **24**, 175 (2012).

[97] G. Amarandei, P. Beltrame, I. Clancy, C. O'Dwyer, A. Arshak, U. Steiner, D. Corcoran, and U. Theile, Soft Matter **8**, 6333 (2012).

[98] S. A. Safran, Adv. Phys. **48**, 395 (1999).